

1 “ACCEPTED FOR PUBLICATION IN GLOBAL BIOGEOCHEMICAL CYCLES.
2 COPYRIGHT (2010) AMERICAN GEOPHYSICAL UNION. FURTHER
3 REPRODUCTION OR ELECTRONIC DISTRIBUTION IS NOT PERMITTED.”

4 5 **High productivity in an ice melting hotspot at the eastern** 6 **boundary of the Weddell Gyre**

7 W. Geibert*, P. Assmy, D.C.E. Bakker, C. Hanfland, M. Hoppema, L. Pichevin, M. Schröder, J. N.
8 Schwarz, I. Stimac, R. Usbeck, A. Webb

9 * corresponding author: walter.geibert@ed.ac.uk

10 11 **Abstract**

12 **The Southern Ocean (SO) plays a key role in modulating atmospheric CO₂ via physical and**
13 **biological processes. However, over much of the SO, biological activity is iron-limited. New**
14 **in situ data from the Antarctic zone south of Africa in a region centred at ~20-25°E, reveal a**
15 **previously overlooked region of high primary production, comparable in size to the**
16 **Northwest African upwelling region. Here, sea ice together with enclosed icebergs is**
17 **channelled by prevailing winds to the eastern boundary of the Weddell Gyre, where a sharp**
18 **transition to warmer waters causes melting. This cumulative melting provides a steady**
19 **source of iron, fuelling an intense phytoplankton bloom that is not fully captured by monthly**
20 **satellite production estimates. These findings imply that future changes in sea ice cover and**
21 **dynamics could have a significant effect on carbon sequestration in the SO.**

22 **1 Introduction**

23 Oceanic processes are believed to play a pivotal role in glacial-interglacial variations in atmospheric
24 CO₂ [D M Sigman and E A Boyle, 2000]. One key mechanism for changing atmospheric CO₂ is a

25 variable exchange between the deep ocean and surface water, which is likely to be linked to ocean
26 stratification, sea ice cover and deep upwelling at high latitudes [*R F Anderson et al.*, 2009; *R*
27 *Francois et al.*, 1997; *B B Stephens and R F Keeling*, 2000]. Another important factor is the variation
28 in primary production and in the silicon to carbon (Si/C) ratio of organic matter, resulting from
29 changes in growth-limiting conditions [*D A Hutchins and K W Bruland*, 1998; *L Pichevin et al.*, 2009;
30 *O Ragueneau et al.*, 2006; *S Takeda*, 1998]. Iron, which is present only in trace levels in open ocean
31 sea water has repeatedly been shown to be crucial in controlling primary production in regions
32 where upwelling provides major nutrients in excess [*P W Boyd et al.*, 2007].
33 The Weddell Gyre (WG), which constitutes the world's largest coherent deep ocean-atmosphere
34 interface, unifies all the potential oceanic CO₂-regulating mechanisms. Furthermore, the effects of
35 changes in nutrient uptake on atmospheric CO₂ drawdown are far more efficient in the WG than in
36 other areas of the SO [*I Marinov et al.*, 2006]. The anticipation that sea-ice cover and ice melt
37 patterns could change in the future increases the urgency to understand the role of the WG and
38 seasonal ice cover in regulating atmospheric CO₂.

39 **1.1 The Eastern Weddell Gyre**

40 While clearly being a crucial factor in global climate [*M Hoppema*, 2004], the WG is also a
41 particularly intricate piece of the puzzle, because of high inter-annual variability in sea-ice cover and
42 spatial structure [*L de Steur et al.*, 2007; *D G Martinson and R A Iannuzzi*, 2003], and limited
43 accessibility. One of the least investigated parts of the WG is its eastern boundary, a transition zone
44 to the Antarctic Circumpolar Current (ACC), at approximately 20-35°E, south of 55°S.

45 The few oceanographic data from the Eastern Weddell Gyre (EWG)/ACC boundary region [*V V*
46 *Gouretski and A I Danilov*, 1993; *M Schröder and E Fahrbach*, 1999] have shown that water masses
47 with different characteristics and momentum meet here. Remotely sensed sea surface temperature
48 data reveal a colder northern and a warmer southern regime in the WG, together with a north-south
49 (N-S) oriented EWG/ACC boundary in temperature at approximately 25°E (Figure 1b). This N-S

50 oriented boundary is also seen in a southward deflection of the oceanic frontal system [A H Orsi et
51 al., 1995], which coincides with regional seafloor topography (Figure 1a).
52 According to modelling studies, the EWG region receives a certain, but not exceptionally high
53 amount of melt water from icebergs [J I Jongma et al., 2009; M P Schodlok et al., 2006], which
54 would mainly originate in the Lazarev Sea, the Riiser-Larsen Sea, and possibly the Western part of
55 the Weddell Gyre [R M Gladstone et al., 2001]. In contrast, remote sensing data and episodic
56 reports from shipboard observations confirm the common occurrence of icebergs in the EWG
57 region, whereas less icebergs are observed further east [J Tournadre et al., 2008]. Icebergs have
58 been shown to affect productivity in the Southern Ocean, though the actual effect depends on local
59 conditions. Icebergs can lead to decreasing productivity by secondary effects on the pack ice [K R
60 Arrigo et al., 2002], or they can stimulate phytoplankton growth [K L Smith et al., 2007][J N Schwarz
61 and M P Schodlok, 2009].

62 **1.2 Contrasting indicators of productivity at the EWG/ACC boundary**

63 Long-term averages of ocean productivity from inverse modelling based on nutrient distributions,
64 indicate that exceptionally high downward fluxes of organic carbon and large fluxes of silica are a
65 permanent feature at this boundary [R Usbeck et al., 2002] (Figure 2a), in agreement with historic
66 data from whale catches [C T Tynan, 1998] (Figure 2b). Whereas this maximum in ocean primary
67 production was displayed in productivity maps prior to the satellite era [W H Berger, 1989], it has
68 been less pronounced in recent studies using satellite data, probably because of the tendency to
69 use monthly composites or long-term means [R Schlitzer, 2002; W O Smith and J C Comiso, 2008],
70 and because the likelihood of glimpsing high productivity amid patchy sea-ice cover and frequent
71 cloud cover is low from satellite as compared to ship surveys. The WG in general has been shown
72 to produce anomalously low particle fluxes to the deep ocean and the sediment due to enhanced
73 dissolution, which prevents simple conclusions from the underlying sedimentary patterns from being
74 drawn [W Geibert et al., 2005; A Leynaert et al., 1993; R Usbeck et al., 2002].

75 If the occurrence of markedly elevated productivity levels in the EWG-ACC transition zone could be
76 verified by in-situ measurements, the question of what mechanisms support such a bloom in the
77 open ocean, remote from any obvious iron source, would remain. Expedition ANT XX/2 was carried
78 out on the icebreaker RV “Polarstern”, to generate an in situ biogeochemical dataset to complement
79 indirect information from modelling and remote sensing techniques. Our study combines
80 measurements of nutrient and dissolved inorganic carbon profiles, data on physical oceanography,
81 the distribution of chlorophyll-a as seen in depth profiles and from remote sensing, the chemical
82 composition of particles collected at the sea surface, the species composition of phytoplankton, and
83 the distribution of the naturally occurring radioisotopes ^{234}Th and $^{227}\text{Ac}_{\text{xs}}$ to quantitatively capture the
84 regional distribution of productivity, and to identify the controlling processes. We compare our results
85 to previous findings and related studies in order to demonstrate the recurring nature of the observed
86 phenomenon.

87 The expedition to the WG took place from 24 November 2002 to 23 January 2003, consisting of a
88 western transect in full or partial ice cover (Figure 3a), and an eastern transect at the EWG/ACC
89 boundary at 17-23°E (Figure 3b). Here, we focus on the latter, which had some sea ice remaining at
90 the southernmost stations, but ice-free conditions in the northern part [D C E Bakker *et al.*, 2008].

91 **2 Methods**

92 **2.1 Sampling and analysis**

93 *2.1.1 Nutrients*

94 Polyethylene (PE) 50 mL bottles were used to collect sub-samples from Niskin bottles for nutrient
95 analysis. The PE bottles were rinsed three times with the sample water. The samples were poisoned
96 with 105 µg/mL mercuric chloride (HgCl_2), stored at 4°C and analysed at the home laboratory seven
97 months after sampling. This preservation method has been shown to be successful for the storage
98 of nutrient samples for up to two years [G Kattner, 1999]. A Technicon autoanalyser II was used to
99 measure the concentrations of Si, NO_x^- , NO_2^- and NH_4^+ using standard techniques [K K Grasshoff,

100 *K.; Ehrhardt, M., 1983*]. All the samples were analysed in duplicate and the average difference of the
101 duplicates from the mean was 0.23% for NO₃⁻ and 0.26% for Si.

102 2.1.2 Oxygen

103 Samples for oxygen analysis were the first to be drawn from the Niskin bottle unless
104 chlorofluorocarbon (CFC) samples were taken. Volume calibrated glass bottles of ~120 ml were
105 used. A piece of Tygon tube was attached to the outlet tap of the Niskin bottle to allow the water to
106 enter the sample bottle with minimum air contact and turbulence. The sample was allowed to
107 overflow up to three times the bottle volume and the temperature of the seawater was then
108 measured. The oxygen was chemically fixed and the bottles were capped and shaken. Samples
109 were analysed using the standard Winkler method [*K K Grasshoff, K.; Ehrhardt, M., 1983*] within 12
110 hours of collection. Whole bottle titrations were performed as recommended for WOCE [*C H*
111 *Culberson, 1991*]. The titration process was automated and the endpoint calculated using an
112 electronic burette and photometer linked to a computer (SiS GmbH Dissolved Oxygen Analyser).
113 Duplicate samples were drawn and analysed for 10 % of all the samples. The analytical precision of
114 these duplicates was 0.45%.

115 2.1.3 Pigments

116 Phytoplankton samples were taken by filtering sea-water samples from Niskin bottles onto pre-
117 combusted GF/F filters. All samples were taken in duplicate or triplicate. Filters were stored in liquid
118 nitrogen until analyzed in the home laboratory. Phytoplankton pigment concentration was measured
119 by high performance liquid chromatography (HPLC)[*S W Wright et al., 1991*]. The HPLC system
120 comprised a Waters 600E Controller, Waters 717 plus Autosampler, Techlab column oven
121 (maintaining a temperature of 30 °C), Waters Spherisorb ODS-2 column (250 x 4.6 mm, 5 µm
122 packing) and Waters 996 Photo Diode Array detector. All solvents were HPLC-grade (Chromoscan
123 Inc.). Pigments were extracted by placing the filter together with 20 µl internal standard solution
124 (canthaxanthin, Roche pharmaceuticals, in 100% DMF), 0.5 mm zirconia beads (Biospec Products

125 Inc.) and 600 µl > 99% acetone into a conical-tipped vial and shaking for 50 seconds at 50,000 rpm
126 in a Mini-Bead Beater™ (Biospec Products Inc.). Extracted pigments were separated from filter
127 debris by centrifugation at 3500 rpm for 3 minutes, followed by 1 minute at 10,000 rpm, with the
128 centrifuge cooled to 0°C. 180 µl of the eluent were added to a 250 µl glass insert within a sprung
129 brown-glass HPLC vial together with 45 µl 1M ammonium acetate buffer, and 180 µl of this final
130 solution was injected into the HPLC. The HPLC chlorophyll-a peaks were calibrated against pigment
131 standards from the International Agency for ¹⁴C Determination, Denmark.

132 Optical measurements of chlorophyll-a (chl-a) were obtained in situ with a Seapoint Fluorometer at a
133 vertical resolution of <1 m. The optical measurements (F, in arbitrary units) from the nearest 1 m
134 depth-bin of the CTD upcast were calibrated against the discrete HPLC measurements, giving the
135 the linear equation

$$136 \text{ chl-a} = 168.4 [\pm 6.54] * F \quad (\text{Equation 1})$$

137 The linear correlation of HPLC and in-situ fluorometer data was found to explain 76% of the variance
138 (n=61). Some evidence of time dependence was found, with fluorescence efficiency apparently
139 depressed during high solar zenith, but the difference was insufficient to justify the application of a
140 time-dependent calibration. The reported values are optical measurements by fluorometry, from 1 m
141 depth-binned downcasts, as calibrated using Equation 1.

142 *2.1.4 Large-volume phytoplankton samples as obtained by a continuous flow centrifuge* 143 *(composition of suspended matter, species overview)*

144 At selected stations, large-volume samples of particulate matter were taken from the ship's sea
145 water supply with a continuous flow centrifuge (Padberg Z61), fitted with a trace-element clean
146 introduction and separation system [U Schussler and K Kremling, 1993]. With this system, particles
147 are deposited at 17,670 x g onto an acid-cleaned Teflon® sheet. Sample volumes (868-3507 L)
148 were recorded with a flow meter. The samples were freeze-dried, then analysed for C, N and S
149 contents. Biogenic silica content was determined by continuous leaching [P J Mueller and R

150 *Schneider*, 1993]. Total iron concentrations were determined by Inductively Coupled Plasma Optical
151 Emission Spectroscopy (ICP-OES). The procedural blank contributed 0.6-2.5% to the values.
152 Reproducibility was monitored by reference material HISS-1 (marine sediment from Hibernia Shelf,
153 National Research Council Canada). Control samples were run after partial and complete cleaning
154 of the diatom frustules from organics and clay to exclude external contamination. A potential
155 contamination on some of these samples was also excluded via inspection by SEM. Aliquots of
156 the phytoplankton samples were investigated for species composition in order to identify potentially
157 bloom-forming diatoms (details below).

158 *2.1.5 Physical oceanography*

159 Temperature and salinity were recorded with a Seabird SEACAT SBE 19 instrument. Here, we
160 report 5 m averages. Bottle data were related to the salinity and temperature of the nearest 5 m data
161 point. A comparison of the physical data with that from another CTD-instrument, which was operated
162 in parallel and continuously calibrated against sea water standards (Schröder et al., in prep.) yielded
163 excellent agreement.

164 *2.1.6 Radionuclides*

165 The $^{234}\text{Th}/^{238}\text{U}$ disequilibrium in productive surface waters has proven to be a useful indicator of
166 particle export from the euphotic zone [*J K Cochran and P Masque*, 2003; *N Savoye et al.*, 2006].
167 We measured the disequilibrium according to an established method [*M M Rutgers van der Loeff*
168 *and W S Moore*, 1999]. Briefly, water samples of 20 L were filtered (142 mm diameter, 1 μm pore
169 size Nucleopore) immediately after recovery. The filters were dried and folded, and particulate ^{234}Th
170 was counted directly on the filters via beta counting while on board. Appropriate corrections for self
171 absorption were applied. In the dissolved fraction, a precipitate of MnO_2 was generated, which was
172 quantitatively recovered on filters (analogue to the particulate fraction). The counting procedure was
173 identical to that used for the particulate fractions. Again, suitable self-absorption corrections were
174 applied. No external yield tracer was used. A set of deep samples (400 m) in full radioactive

175 equilibrium was taken to calibrate the method. Quantitative recovery was controlled by monitoring
176 ^{234}Th equilibrium in the deepest sample. After the cruise, all samples were re-counted after decay of
177 ^{234}Th for the determination of background contributions from other nuclides. ^{238}U was calculated
178 from salinity [*M M Rutgers van der Loeff and W S Moore, 1999*]. The integrated deficit of ^{234}Th was
179 taken as a measure of particle export. Based on a given $C_{\text{org}}/^{234}\text{Th}$ ratio, ^{234}Th depletion could be
180 converted into an estimate of C_{org} export. A substantial component in the calculation of ^{234}Th -based
181 carbon export is the choice of an appropriate model for representing steady state or non-steady
182 state conditions [*N Savoye et al., 2006*]. In our case, we selected a special version of non-steady
183 state conditions, assuming that particle export during the winter season under the ice was negligible;
184 therefore ^{234}Th would be in equilibrium with ^{238}U . The assumption that ^{234}Th is close to secular
185 equilibrium during the winter months is supported by our findings from the ice-covered transect at
186 0°E during the same expedition. Sea-ice retreat occurred during December, which allows some
187 export to have happened several weeks before sampling, while our model implicitly assumes that
188 export production prior to sampling was insignificant. In the event that export production was actually
189 high before the austral spring, the ^{234}Th export estimates will therefore be subject to a negative bias,
190 i.e. this method underestimates production. The resulting model simply translates the integrated
191 deficit of ^{234}Th (measured in disintegrations per minute, dpm) into an export of C by means of the
192 $C_{\text{org}}/^{234}\text{Th}$ ratio. The $C_{\text{org}}/^{234}\text{Th}$ ratio in particles was obtained by direct measurements of particulate
193 ^{234}Th ($^{234}\text{Th}_{\text{part}}$), combined with C contents for the individual samples that were derived from
194 fluorometrically determined chlorophyll-a (chl-a). The relation $C_{\text{org}}/\text{chl-a}$ was determined by means of
195 discrete C_{org} samples from the large volume centrifuge (as described above). Based on this relation,
196 particulate C_{org} was calculated for each ^{234}Th value. The resulting $C_{\text{org}}/^{234}\text{Th}$ values on particles were
197 found to be highly variable, from 1.2 to 80.0 $\mu\text{mol } C_{\text{org}}/\text{dpm } ^{234}\text{Th}$, with an average of 11.7 μmol
198 $C_{\text{org}}/\text{dpm } ^{234}\text{Th}$. By multiplying the ^{234}Th deficit of a depth interval with the respective $C_{\text{org}}/^{234}\text{Th}$ ratio
199 on particles, a C_{org} export could be derived. Adding up all positive C_{org} exports at the surface, we can
200 derive an integrated C_{org} export at the ^{234}Th stations. Negative export values may occur due to re-
201 mineralization of ^{234}Th at greater depths, which leads to excess ^{234}Th [*R Usbeck et al., 2002*].

202

203 $^{227}\text{Ac}_{\text{xs}}$ is a tracer that can be used to reveal inputs of deep water to the surface in open ocean
204 waters. This isotope, with a half-life of 21.77 years, has a very dominant source at the deep-sea
205 floor [W Geibert *et al.*, 2008]. Its half-life does not usually allow it to reach the upper water column [Y
206 Nozaki, 1984; 1993], and the Weddell Gyre is a remarkable exception to this rule, illustrating the
207 rapid upwelling of deep waters. Only surface waters that have very recently been formed through
208 upwelling from greater depths can display high $^{227}\text{Ac}_{\text{xs}}$ values. Surface waters in the WG have been
209 found to contain a unique signature of $^{227}\text{Ac}_{\text{xs}}$ of $\sim 0.5 \text{ dpm/m}^3$, whereas values for ACC surface
210 waters are near 0.25 dpm/m^3 [W Geibert *et al.*, 2002]. ^{227}Ac was collected in samples from the ship's
211 sea water supply. Two sequential polypropylene filter cartridges coated with manganese dioxide
212 were used to extract ^{227}Ac from the sea water. The filter cartridges were acid-leached with 6 N
213 hydrochloric acid in a Soxhlet extraction system, in the presence of a $^{229}\text{Th}/^{225}\text{Ac}$ spike. The
214 chemical separation and detection of ^{227}Ac followed previously published procedures [W Geibert and
215 I Vöge, 2008; W Geibert *et al.*, 2002].

216 2.1.7 CO_2

217 The description of CO_2 dynamics from the expedition has already been published [D C E Bakker *et*
218 *al.*, 2008]. In the present study, we use the TCO_2 data to constrain C drawdown independently from
219 the nutrient budget. Briefly, TCO_2 is the sum of all inorganic carbon species dissolved in the ocean,
220 also known as DIC. It is measured using the precise coulometric technique. All samples were
221 measured in duplicate or triplicate. The precision was estimated to be $\pm 1.8 \mu\text{mol kg}^{-1}$, while the
222 accuracy, set by internationally recognized Certified Reference Material (CRM), was $\pm 2.5 \mu\text{mol kg}^{-1}$.

223 2.1.8 Species composition

224 The species composition is based on the relative contribution of each species/genus with respect to
225 the total community and relies on semi-quantitative abundance estimates. This information on
226 species composition was obtained from the large-volume centrifuge samples (see method

227 description above), which does not preserve species without a hard shell. The microscopic
228 examination of the large-volume centrifuge samples is therefore biased towards diatoms that are
229 encased by resistant silica cell walls. However, since diatoms are the almost exclusive bloom
230 formers and the major exporters of organic matter to subsurface waters in the Southern Ocean, they
231 are a good indicator of the productivity regime prevalent at the respective sites of this survey.
232 An aliquot of the plankton samples was preserved with hexamine-buffered formaldehyde at a final
233 concentration of 2%. Samples were settled in 3 ml sedimentation chambers (Hydrobios, Kiel,
234 Germany) for at least 2 hours. Cells were identified and enumerated using inverted light and
235 epifluorescence microscopy (Axiovert 200, Zeiss, Oberkochen, Germany) according to the method of
236 Utermöhl [*H Utermöhl*, 1958]. Organisms were counted at magnifications of 200–400x according to
237 the size of the organisms examined.

238 **2.2 Data processing and calculations**

239 *2.2.1 Calculating the amount of sea-ice meltwater*

240 At the time of sampling, the sea-ice cover was already absent at the EWG/ACC boundary [*D C E*
241 *Bakker et al.*, 2008] for all but the southernmost stations. A corresponding melt-water signal could
242 be identified as decreased salinity, combined with elevated sea surface temperatures (Figure 4). In
243 order to assess the input of melting ice quantitatively, we use the salinity minimum at the surface
244 compared to the underlying Winter Water (WW, salinity here 34.05). In Table 1, we report the
245 thickness of melting sea-ice required to explain the integrated salinity deficit at the sea surface
246 (same transect as Figure 4, see track in Figure 3, right hand side). The calculation is based on a
247 sea-ice-salinity of 5, as estimated from earlier sea-ice salinity profiles from the WG [*H Eicken*, 1992].
248 The average density of sea-ice with snow cover was assumed to be 815 g/L, based on a keel-to-sail
249 ratio of 4.4, as reported by [*A P Worby et al.*, 2008].

250 2.2.2 Assessing productivity

251 The synoptical approach of our study allows us to constrain production in various ways. Here, we
252 explain the approaches, compare the respective results, and summarize the implications for
253 bioproductivity. Briefly, the assessment of productivity is based on (1) the integrated depletion of
254 nutrients, (2) the balance of the carbonic acid system, (3) pigment distribution, both from (a) stocks
255 found in-situ (b) a chl-a based in situ primary production algorithm, and from (c) a satellite
256 perspective, and (4) with a comparatively coarse resolution, we can assess export production by
257 combining ^{234}Th data and the data from large-volume centrifuge samples. The results are presented
258 in Table 1; we discuss the different approaches below.

259 (1) In a similar approach to [M Hoppema et al., 2002], we first determine the nutrient concentration
260 prior to the onset of the bloom. We assume that the Winter Water (WW) at 23°E ($T < -1.76^\circ\text{C}$)
261 represents the initial conditions; the WW is found here as a temperature minimum below the warmer
262 surface layer (Figure 4). We obtain $28.7 \pm 0.4 \mu\text{mol/kg}$ for NO_3^- ($n=10$) and $61.7 \pm 1.8 \mu\text{mol/kg}$ for Si
263 ($n=10$) as the starting point. We attribute deficits in nutrient concentrations compared to the
264 concentration in WW to primary production. Based on the vertical distribution of nutrient
265 concentrations, we can calculate an integrated deficiency for NO_3^- and Si, respectively, in mmol/m^2 .
266 Assuming a constant Redfield value (106:16) for the molar C:N uptake ratio in the Weddell Sea [M
267 Hoppema and L Goeyens, 1999], as supported by the findings from large volume particulate
268 samples from this cruise, we calculate the organic carbon (C_{org}) production at 23°E. C_{org} production
269 in the bloom is consistently found to be about $2000 \text{ mmol} \cdot \text{m}^{-2}$, silicon production is about 1000
270 $\text{mmol} \cdot \text{m}^{-2}$. The values integrate production for the whole productive season up to the sampling date.
271 They reflect the net community production (NCP), which is lower than the net primary production.

272

273 (2) We can calculate the difference between the sum of all dissolved inorganic carbon species
274 (TCO_2) in WW ($2183.52 \pm 8.11 \mu\text{mol kg}^{-1}$, $n=8$, for $T \leq -1.76^\circ\text{C}$ and latitude $> -65^\circ\text{S}$) and measured
275 TCO_2 profiles above WW. The depth-integrated difference of TCO_2 compared to WW after
276 normalization to a salinity of 35 can then be interpreted as carbon consumption by primary

277 production, again reflecting NCP. These values are given for comparison with the production as
278 derived from nutrients, but the uncertainty associated with the underlying assumptions should be
279 taken into account. In particular, this approach does not consider exchange with the atmosphere, so
280 values will become less reliable with increasing elapsed time since the onset of spring production.
281 Uptake of CO₂ from the atmosphere will generally tend to cause a slight underestimate of
282 production. We also implicitly neglect the potential effect of calcification. We assume the presence of
283 a WW layer that is homogenous in TCO₂, irrespective of the latitude, while in fact some of the
284 reported standard deviation of the WW signal may be due to a latitudinal trend. Moreover, the
285 normalisation procedure, necessary to correct for dilution by sea ice melting, neglects the TCO₂
286 content of sea ice, possibly also leading to an underestimate of production. While these error
287 sources might cause a possible bias of the primary production estimate, most likely towards an
288 underestimate, the potential bias is smaller than the large signal we observe.

289

290 (3 a) Measured in-situ chlorophyll-a (chl-a) fluorescence was calibrated against chl-a as measured
291 by HPLC on discrete samples (see methods). No filtered samples were taken for C_{org} analysis.
292 Instead we used large-volume centrifuge samples for C_{org} and individual chl-a values from the
293 nearest in-situ fluorometer measurement to calculate an empirical C_{org}-chl-a relationship . The
294 values presented in Table 1 were obtained by vertically integrating the stock of chl-a, and multiplying
295 this value with the empirical factor

$$296 \quad C_{part} [\mu\text{mol} / L] = 0.0104 * chl - a [ng / L] \quad (r^2=0.84, n=10)$$

297 This corresponds to a C/chl-a ratio of 125 mg/g, which is well within the range of previously reported
298 data from the Southern Ocean [I A Garibotti et al. 2003]. If grazing and mortality/export were
299 negligible, and chl-a was close to zero during winter, then the depth-integrated chl-a stock would
300 represent the cumulative production for the sampling season. If phytoplankton cells were released to
301 the water from melting sea-ice and were retained in the surface waters, then this method yields an
302 overestimate of seasonal production. If export has taken place, as we explore below, this value
303 underestimates true production.

304

305 (3b) Daily primary production was calculated for each station using the vertically-generalised
306 production model [M J Behrenfeld and P G Falkowski, 1997]. Surface chl-a was taken from the
307 calibrated fluorometry profiles at 10 m, daily insolation from the standard 9 km SeaWiFS product,
308 P_{opt}^B , the maximum carbon fixation rate within the water column, was calculated using CTD-
309 measured surface temperatures[M J Behrenfeld and P G Falkowski, 1997], euphotic zone depth
310 was calculated using each chl-a profile[A Morel and J F Berthon, 1989] and the number of daylight
311 hours was calculated [J T O Kirk, 1994]. Daily production was multiplied by 28 days to give an
312 estimate of seasonal production comparable to the nutrient results.

313

314 (3c) 8-day production estimates provided by the NASA-affiliated Ocean Productivity Team were
315 taken for the four closest weeks during which each pixel was cloud- and ice-free. For each station,
316 these four daily productivity values were multiplied by 7 days and summed to give a 28-day
317 production estimate for comparison with the other methods.

318

319 (4) Because of the 24-day half-life of ^{234}Th , the ^{234}Th -derived export production reflects only the
320 particles that have recently been removed from the surface. Therefore, they should be similar or
321 lower than the estimates obtained by other approaches. With the exception of station PS63/128-1,
322 which is anomalously high, the ^{234}Th -based export production is lower than the nutrient-derived
323 primary production, while confirming the exceptional productivity levels in the bloom.

324 2.2.3 Exploring the differences between the productivity estimates

325 The estimates from nutrient depletion are considered to be very reliable, as long as the surface
326 waters are fed by WG Winter Water (WW) or the local ACC waters, which have very similar nitrate
327 contents. This assumption holds for the entire bloom area, which yields consistent production values
328 from all calculation approaches. It is less valid for the southernmost stations, which are located in
329 the vicinity of the Antarctic Coastal current that brings waters from the east.

330 The production data from TCO₂ should not be taken as absolute values, as uptake from the
331 atmosphere may have altered them, causing an underestimate [D C E Bakker et al., 2008]. They
332 also respond strongly to the assumptions of a WW origin, as nearby ACC water has a different TCO₂
333 content to WW. Where the prerequisites are met, the production data from TCO₂ clearly confirm the
334 findings from the nitrate distribution.

335 The production estimates from in-situ chlorophyll-a (chl-a) (Figure 4) depend on the accuracy of the
336 fluorometer calibration, and on the organic carbon (C_{org}) versus chl-a conversion factor, which has
337 been determined using a limited number of stations. This adds some uncertainty to the absolute
338 production results, while being a reliable indicator for qualitative changes. The in situ estimates of
339 the Vertically Generalized Production Model (VGPM) are significantly, but not tightly correlated with
340 in situ, depth-integrated chl-a stocks ($r^2 = 0.426$, $n = 27$). The major uncertainty for this method is
341 the length of the productive season, combined with temporal variability in surface chl-a. If the
342 calculations are repeated for an assumed productive season lasting 90 days, then the VGPM
343 estimates agree well with the nutrient-based estimates, whereas for a 28 day productive season, the
344 VGPM values are much lower than the nutrient-based estimates (VGPM = nutrient • 0.2243[± 0.03]
345 + 245[± 42], $r^2 = 0.637$, $n = 28$), suggesting that the satellite did not capture the highest chl-a values.
346 Both in situ and satellite-based VGPM results are affected by uncertainty in the maximum rate of
347 photosynthesis (P_{opt}^B), which ranged from 1.1 to 6.6 mg C (mg chl-a)⁻¹ hr⁻¹, when calculated using
348 the CTD data [M J Behrenfeld and P G Falkowski, 1997]. This is within the range reported
349 previously for low temperature waters [M J Behrenfeld and P G Falkowski, 1997]. Another critical
350 factor affecting satellite-derived estimates is the correlation between surface chl-a and depth-
351 integrated chl-a, which was good for this dataset ($r^2 = 0.624$, $n=34$), i.e. there was no 'invisible' deep
352 chlorophyll maximum at the time of sampling. ²³⁴Th-export data agree well with the other production
353 data, as they are expected to be a certain fraction of the primary production. In summary, all
354 production estimates yield comparable results for the bloom area, where the model assumptions are
355 met best.

356 **3 Results**

357 The complete in-situ data and results on species composition can be obtained from the Pangaea
358 data base (<http://doi.pangaea.de/10.1594/PANGAEA.726958>)

359 **3.1 Sea ice and primary production**

360 The results as reported in Table 1 indicate a maximum of melt water at three stations just north of
361 60°S, corresponding to an average sea-ice thickness of ~130 cm. We compare this observed value
362 to the previously reported local sea ice thickness. For the EWG in winter, on a >10 year average,
363 typically 89% of the sea surface is covered by 54 ± 37 cm sea ice, corresponding to 48 cm for 100%
364 cover [A P Worby *et al.*, 2008]. The observed melt water of up to 130 cm therefore represents 2.7
365 times the typical sea ice thickness for this region. We must consider the possibility that the
366 freshwater lens has spread horizontally, in which case the factor 2.7 is an underestimate of the
367 actual meltwater contribution. At most stations in the region influenced by meltwater, no notable
368 mixed layer was present, as large gradients in temperature and salinity were observed even in the
369 uppermost layers (Figure 4c, Figure 4d). Most chlorophyll maxima in the bloom region were seen
370 between 20 and 40 m depth (Figure 4b).

371 Primary production was estimated using a variety of approaches based on independent datasets,
372 detailed in the methods section. An intense bloom with substantial productivity is detected by all
373 approaches (Table 1). The nutrient distribution (Figure 4) locates the most intense bloom between
374 62.5°S and 56.0°S, coinciding with the region of maximum meltwater input. The production of
375 organic carbon (C_{org}) in the bloom as indicated by nitrate deficits is consistently found to be about
376 $2000 \text{ mmol} \cdot \text{m}^{-2}$, (Table 1). Silica production is about $1000 \text{ mmol} \cdot \text{m}^{-2}$. These values integrate
377 production for the whole productive season up to the sampling date, and they reflect the net
378 community production (NCP), which is lower than the net primary production.

379 The well constrained N-S extent of the bloom is approximately 600 km; the E-W extent was
380 estimated to be at least 1000 km in January, based on the surface distribution of chl-a (Figure 3),
381 which means the bloom covers an area of $>600,000 \text{ km}^2$, about as large as the Northwest African
382 upwelling region at maximum extent [P Helmke *et al.*, 2005].

383 The productivity levels (2000 mmol/m² in a period of ~1 month) are comparable to those of blooms
384 found in naturally iron-fertilized coastal or island Antarctic environments, and they are higher than in
385 artificially iron-fertilized patches [*D C E Bakker et al.*, 2007]. The observed bloom also resembled
386 natural [*S H Kang and G A Fryxell*, 1993; *V Smetacek et al.*, 2002] and artificially iron-induced
387 blooms [*P Assmy et al.*, 2008; *P Assmy et al.*, 2007; *A Tsuda et al.*, 2003] in the prevalence of
388 *Chaetoceros* species within the bloom area.

389 **4 Discussion**

390 **4.1 High productivity and low salinity in the EWG**

391 Our results present strong evidence for the existence of substantial bioproductivity at the EWG/ACC
392 boundary. The previous identification of such a region by inverse modelling [*R Usbeck et al.*, 2002],
393 high biogenic silica fluxes to the underlying sediment [*W Geibert et al.*, 2005], and high whale
394 abundances [*C T Tynan*, 1998] strongly suggests that this is a recurrent feature, though variable in
395 location and extent, because the location of the boundary wanders longitudinally between years
396 (indicated by patchiness around the 0.5°C isotherm in Figure 1).

397 The salinity minimum in the EWG, which is too pronounced to be fed from any local water mass, has
398 not only been observed in this season, but it has also been found in other studies, e.g. expedition
399 Polarstern ANT XVI/3 [*M Boye et al.*, 2001], or the recent ANDREX study [DCEB, pers. comm.]. We
400 therefore conclude that excess melting ice is also a recurrent phenomenon in the EWG.

401 Our results show that the productivity is linked to melting ice at the sea surface. The link between
402 melting sea-ice and phytoplankton blooms has been described previously [*G Savidge et al.*, 1996; *W*
403 *O Smith and D M Nelson*, 1985; *S Sokolov*, 2008]. However, it has been demonstrated that
404 stratification due to sea ice alone is not sufficient to generate large phytoplankton blooms [*U V*
405 *Bathmann et al.*, 1997]. Consequently, we must not only consider the role of melting sea ice for
406 increased stratification of surface waters, but also for the enhanced supply of limiting micronutrients,
407 especially iron. We will therefore focus our discussion on two specific aspects of the observations.
408 First, we explore mechanisms that might explain why the EWG/ACC boundary receives consistently

409 more freshwater (from sea ice or icebergs) than other regions of the SO, and second, we investigate
410 how this may relieve iron limitation.

411 **4.2 Enhanced supply of ice to the EWG boundary**

412 Freshwater supply to the EWG/ACC boundary is controlled by sea-ice, icebergs and precipitation
413 (mainly onto sea-ice). Sea-ice transport in the WG generally follows wind forcing, which results in a
414 general pattern of eastward transport in the northern WG [*N Kimura, 2004; J Uotila et al., 2000*], see
415 Figure 5b. For most parts of the WG, the atmospheric circulation patterns roughly coincide with the
416 ocean circulation, which means that sea-ice remains within the same water mass. The EWG/ACC
417 boundary is an exception to this rule. Here, a longitudinal boundary in surface water masses is
418 found at $\sim 25^\circ\text{E}$ (Figure 1), across which sea ice drifts under wind forcing (see Figure 5). This
419 situation holds not only in spring, but also persists in winter, then slightly further north-eastwards,
420 leading to enhanced sea-ice melting rates at the EWG/ACC boundary. With ice drift velocities of 15
421 cm/s [*N Kimura, 2004*] and an average ice thickness of 48 cm [*A P Worby et al., 2008*],
422 approximately 42 L of sea ice volume cross each metre of this boundary per minute.

423 Icebergs might be expected to follow the circulation of the underlying water masses, as they
424 penetrate to considerable water depths, whereas the cross-sectional area exposed to wind is
425 comparatively small. However, a combination of observational data and modelling has shown that
426 even large Antarctic icebergs follow the wind-drifted sea-ice in which they are enclosed [*C Lichey
427 and H H Hellmer, 2001*]. Therefore, a closed sea-ice surface in the winter months also means wind-
428 driven icebergs, which are exposed to higher water temperatures at the EWG/ACC boundary,
429 representing a permanent melting hotspot for wind-drifted ice, as depicted in Figure 5.

430 This advective mechanism explains why the eastern rim of the Weddell Gyre consistently receives
431 an excess of freshwater from melting ice, potentially both icebergs and sea-ice.

432 In order to disentangle the proportions of sea-ice vs. icebergs, we compare our salinity data to a
433 recent modelling study [*J I Jongma et al., 2009*]. Jongma et al. have investigated the potential
434 salinity decrease resulting from melting icebergs in the Southern Ocean. In the region that is

435 affected most by melting icebergs according to their study, Jongma et al. report a salinity decrease
436 of up to 0.3 units, with typical values in the WG of around 0.1. In contrast, we observe a salinity
437 decrease of up to 1.5 units compared to local water masses. We conclude that, from a modelling
438 perspective, icebergs alone would not be sufficient to produce the salinity minimum found in the
439 EWG, and sea-ice must be the main actor. There is, however, episodic shipboard evidence of high
440 iceberg densities in the region, which partly agrees with satellite observations that suggest a
441 decrease in iceberg density east of the EWG/ACC boundary [*J Tournadre et al., 2008*], which would
442 be consistent with increased iceberg melting here. Still, we conclude that melting of excess sea-ice
443 is the main reason for the low salinity in the EWG.

444 This contributes to the persistence of high productivity at this specific location by creating stratified
445 conditions. However, primary production also requires the micronutrient iron, which has repeatedly
446 been found to be limiting in Southern Ocean environments. Therefore, we investigate potential iron
447 sources in the following section.

448 **4.3 Potential Iron Sources**

449 In particulate plankton samples in the bloom area, we measured Fe/C ratios of $2 \cdot 10^{-4}$ mol mol⁻¹
450 (Table 1). The observed values for Fe/C ratios are exceptionally high for an open ocean system,
451 which are usually expected to be in the order of 10^{-5} mol mol⁻¹ or less [*W G Sunda and S A*
452 *Huntsman, 1995; B S Twining et al., 2004*]. We rule out sampling artefacts, because the type of
453 18,000 x g centrifuge used for the collection of particulate samples has previously been shown to be
454 efficient and reliable in collecting trace element samples of marine particulate matter [*U Schussler*
455 *and K Kremling, 1993*]. Inspection of the collected material by Secondary Electron Microscopy
456 (SEM) with energy dispersive analysis of secondary X-rays (EDX) gave no evidence of
457 contaminating terrigenous particles. Approximately 1/20 of the iron was found within the diatom
458 shells, after cleaning from all potential traces of terrigenous matter. As the Fe/C ratio observed here
459 exceeds known values of cellular iron requirements, we consider the possibility that a part of the iron

460 may be present in adsorbed form, or there is a case of “luxury iron uptake and storage” [*W G Sunda*
461 *and S A Huntsman*, 1995].

462 With an organic carbon production of $2000 \text{ mmol} \cdot \text{m}^{-2}$ in the productive layer of the bloom, as derived
463 from nutrient depletion, this corresponds to a particulate iron stock of $400 \text{ } \mu\text{mol m}^{-2}$ (Table 1).

464 Irrespective of the form of iron present in the particulate samples, we conclude that our inferred iron
465 stock of $400 \text{ } \mu\text{mol m}^{-2}$ must be supported by an efficient supply mechanism, as rapid water mass
466 exchange and particle export limit residence times in this dynamic region. Particulate iron export
467 might be less than the 25% ($=100 \text{ } \mu\text{mol m}^{-2}$) suggested by ^{234}Th export data (Table 1), if the Fe/C
468 ratio in exported particles is lower than in suspended matter.

469 Various pathways of iron to the Southern Ocean have been investigated recently, including airborne
470 iron supply from terrestrial sources by dust [*A Martínez-García et al.*, 2009], supply from underlying
471 water masses by deep upwelling and vertical mixing [*N Meskhidze et al.*, 2007], detrital material and
472 mixing effects from islands [*S Blain et al.*, 2007], sea-ice [*D Lannuzel et al.*, 2008], melting icebergs
473 [*E Hegner et al.*, 2007; *R Raiswell et al.*, 2008; *K L Smith et al.*, 2007] or extraterrestrial dust [*K S*
474 *Johnson*, 2001].

475 In order to assess the potential contribution from atmospheric deposition, we use published values
476 of dust or iron in snow. [*D Lannuzel et al.*, 2008] report concentrations of total dissolvable iron in
477 snow on sea-ice of up to 20 nM ($=1.1 \text{ ng/g}$) in the western Weddell Gyre, and similar and lower
478 concentrations are found in Eastern Antarctic sea ice environments [*D Lannuzel et al.*, 2007]. [*M P*
479 *Schodlok et al.*, 2005] calculate with a concentration of 10 ng/g dust in snow, which translates into
480 0.3 ng/g total iron assuming 3% iron in dust, a fraction of which will be dissolvable. No atmospheric
481 iron deposition data are available from the immediate neighbourhood of our study, but aerosol
482 measurements at Neumayer station ($70^{\circ}39'S$, $8^{\circ}15'W$) display strong dust flux maxima in austral
483 summer [*R Weller et al.*, 2008]. Summarizing, we assume an iron concentration of 0.5 ng/g in snow,
484 and a deposition of 100 kg snow per m^2 of sea-ice, after [*A P Worby et al.*, 2008]. This results in a
485 contribution of $50 \text{ } \mu\text{g m}^{-2} \text{ yr}^{-1}$, or $\sim 1 \text{ } \mu\text{mol m}^{-2} \text{ yr}^{-1}$ onto sea ice, 0.25% of the iron stocks we find in the
486 productive layer. Higher iron fluxes may be expected in the ice-free season, but these can only play

487 a minor role for the ice melt related bloom observed here, and these fluxes could still only account
488 for a small fraction of the iron stocks.

489 Deep upwelling is also a source that might be of importance here, as it is prevalent in the WG,
490 especially in its eastern and southern parts, and in the Maud Rise region. Therefore, we will
491 investigate its potential impact based on our data. Typical deep water dissolved iron concentrations
492 in the WG are in the order of 0.2-0.4 $\mu\text{mol}/\text{m}^3$ [*M Boye et al.*, 2001; *P L Croot et al.*, 2004] at 18°E
493 and 6°E, respectively. Vertical transports are high, with annual entrainment rates of deep water on
494 the order of 50 m yr^{-1} [*W Geibert et al.*, 2002; *A L Gordon and B A Huber*, 1990]. Calculating with the
495 higher value (0.4 $\mu\text{mol}/\text{m}^3$), this means an approximate annual supply from below of $\sim 20 \mu\text{mol m}^{-2}$
496 yr^{-1} , which corresponds to only 5 % of the inferred stock in the bloom.

497 We measured $^{227}\text{Ac}_{\text{xs}}$ (Table 1) to investigate whether the origin of the bloom-forming water mass in
498 the EWG is indeed upwelled WG water, or rather water from the ACC. The uniquely high $^{227}\text{Ac}_{\text{xs}}$
499 values known from the WG allow discrimination of WG from ACC waters [*W Geibert et al.*, 2002]
500 despite the alteration in temperature and salinity characteristics by melting ice. Three out of seven
501 $^{227}\text{Ac}_{\text{xs}}$ values at the WG/ACC boundary point to an ACC source ($\sim 0.25 \text{ dpm} \cdot \text{m}^{-3}$), whereas the four
502 other values indicate WG waters or mixtures. The highest $^{227}\text{Ac}_{\text{xs}}$ was in the northernmost part of the
503 WG. Because high productivity spans both ACC and WG surface waters, we can state that deep
504 upwelling in the WG does not seem to be the major iron source that controls this bloom, at least not
505 without sea-ice acting as a transporting agent. We can also infer from the $^{227}\text{Ac}_{\text{xs}}$ -pattern that ACC
506 waters can be found floating on underlying WG waters here.

507 In order to evaluate the potential importance of sea-ice for iron inputs, we take values of sea-ice iron
508 concentrations typical for the western WG from the literature. In early spring, a depth-integrated total
509 iron concentration of 59.4 $\mu\text{mol}/\text{m}^2$ was reported for sea-ice [*D Lannuzel et al.*, 2008]. Observations
510 of iron release associated with the spring melt of sea-ice from the WG at 6°E [*P L Croot et al.*, 2004]
511 confirm that sea-ice is indeed a likely transporting agent for iron in the WG. We concluded in the
512 freshwater budget of our study (section 3.1) that the volume of sea ice delivered to the eastern
513 boundary of the WG is at least 2.7 times higher than the regional average, associated with a higher

514 than average iron supply of $>160.4 \mu\text{mol m}^{-2}$. Cumulative advection of sea-ice to the EWG
515 boundary, followed by melting when encountering warmer ACC waters, therefore accounts directly
516 for 40% of the calculated particulate iron inventory of $400 \mu\text{mol m}^{-2}$. Considering that the sea ice
517 enrichment factor of 2.7 can be an underestimate because the freshwater lens spreads horizontally,
518 and adding the uncertainty of highly variable iron concentrations in sea ice, and then taking into
519 consideration internal recycling, the proposed mechanism can sustain the stock of $400 \mu\text{mol m}^{-2}$ Fe
520 observed here, and create Fe levels that may be temporarily sufficient to alleviate iron limitation.
521 Elevated iron levels in sea-ice may be explained by sorption or uptake of dissolved iron, as depicted
522 in [D Lannuzel *et al.*, 2008]. However, sea-ice can theoretically not contain more iron than delivered
523 by upwelling and atmospheric fluxes together in winter. Therefore, we suggest a mechanism that
524 delivers additional iron into sea-ice during winter, when large icebergs continue melting due to their
525 penetration into deeper water layers (up to > 300 m). This means that they are exposed to warmer
526 waters even during winter, when sea-ice is present and growing. Continuous melting of icebergs in
527 winter will lead to rising fresher and potentially iron-enriched waters from below, in the immediate
528 vicinity of icebergs. This water would spread under the sea-ice as a thin lens of fresher water, where
529 it can refreeze due to its comparatively low salinity, and it can undergo processes of sorption and
530 biological uptake. This hypothesis is consistent with maxima of iron concentrations in the lowermost
531 parts of sea-ice prior to the onset of spring melting [D Lannuzel *et al.*, 2008], and the generally high
532 iron concentration observed in sea ice that is not fully supported by atmospheric deposition and
533 upwelling.

534 **5 Conclusions**

535 Our data highlight the role of melting ice in the enhanced productivity in the EWG. We propose that
536 production is supported by the persistent supply of sea-ice and icebergs to the EWG boundary by
537 wind-driven advection. Here, the encounter with warmer ACC waters results in rapid melting. This
538 melting hotspot causes an enhanced input of iron and salinity-driven stratification of the surface
539 waters. The resulting phytoplankton bloom is extensive and it constitutes a recurrent spring/summer

540 feature that has not been well recognised before in either remote-sensing based estimates or
541 coupled biophysical models.

542 Productivity estimates derived using monthly composited data have been found here to
543 underestimate in situ observations in the bloom region substantially at many stations. Monthly
544 composited remote-sensing data should be used with caution at these latitudes, as intense seasonal
545 blooms such as that described here are likely to be heavily undersampled owing to cloud and ice-
546 cover. The exclusion of partly sea-ice containing pixels during data processing could cause a
547 systematic undersampling of early spring blooms that are related to sea-ice cover, and if sea-ice
548 related blooms released a significant amount of dimethylsulfide, cloud cover could also be coupled
549 to productivity [*R J Charlson et al.*, 1987], causing a bias in satellite observations. The high degree
550 of cloudiness in this region alone means that monthly composites of satellite data represent the best
551 means to study spatial patterns in the data, yet the patchiness caused by cloud cover together with
552 the compositing over four weeks - longer than the residency of peak chlorophyll values during a
553 bloom - together must result in a systematic underestimate of chlorophyll values in monthly satellite
554 products. If such effects were responsible for the mismatch between satellite-based estimates and
555 in-situ data, they would also concern other areas with sea-ice stimulated productivity.

556 A persistent transport mechanism as described here can explain why modelling according to nutrient
557 distributions yields a region of anomalously high export production at the EWG/ACC boundary. It is
558 also consistent with anomalously high opal fluxes to marine sediments in the Indian Sector of the
559 SO [*W Geibert et al.*, 2005], which cannot be linked to upstream islands. The high productivity in the
560 area would also be consistent with elevated whale abundances, as indicated by the historical
561 whaling records. Our results imply that the expected shifts in sea-ice patterns due to global warming
562 are likely to affect the regional distribution of biological productivity. The supply of limiting
563 micronutrients by wind-driven sea-ice and icebergs may have been active in other high latitude
564 HNLC areas, e.g. the Northwest Pacific in the past, and may be active at present at other SO gyre
565 systems.

566

567 **Acknowledgements**

568 MODIS ocean colour and sea surface temperature data were kindly provided by the MODIS Science
569 Team, the Ocean Productivity Group and by the NASA Ocean Color Team. Isabelle Ansorge (team
570 co-ordinator for UCT group), Sandy Thomalla, Rhys Gilliam, Nazeera Hargeyn and the team of
571 Gerhard Kattner contributed substantially to the nutrient and oxygen dataset. Rita Froehlkling
572 assisted with the analysis of particulate samples. WG was supported by DFG projects RU712-4 and
573 GE1118/2-2; he is currently supported by the Scottish Alliance for Geosciences, Environment and
574 Society (SAGES). DCEB and MH were partly supported by the EU IP CARBOOCEAN (511176
575 (GOCE)). PA was supported by the Bremen International Graduate School for Marine Sciences
576 (GLOMAR) funded by DFG (Excellence Initiative). This work would have been impossible without
577 the continuous support of Dieter K. Fütterer, chief scientist of the expedition, and the helpful crew of
578 R/V Polarstern. In remembrance of Wolfgang Dinter.

579

580 **References**

581

582 Anderson, R. F., S. Ali, L. I. Bradtmiller, S. H. H. Nielsen, M. Q. Fleisher, B. E. Anderson, and L. H.
583 Burckle (2009), Wind-Driven Upwelling in the Southern Ocean and the Deglacial Rise in
584 Atmospheric CO₂, *Science*, 323(5920), 1443-1448.

585 Arrigo, K. R., G. L. van Dijken, D. G. Ainley, M. A. Fahnestock, and T. Markus (2002), Ecological
586 impact of a large Antarctic iceberg, *Geophysical Research Letters*, 29(7).

587 Assmy, P., D. U. Hernandez-Becerril, and M. Montresor (2008), Morphological variability and life
588 cycle traits of the type species of the diatom genus *Chaetoceros*, *C-dichaeta*, *J. Phycol.*, 44(1), 152-
589 163.

590 Assmy, P., J. Henjes, C. Klaas, and V. Smetacek (2007), Mechanisms determining species
591 dominance in a phytoplankton bloom induced by the iron fertilization experiment EisenEx in the
592 Southern Ocean, *Deep-Sea Research Part I-Oceanographic Research Papers*, 54(3), 340-362.

593 Bakker, D. C. E., M. C. Nielsdottir, P. J. Morris, J. Venables, and A. J. Watson (2007), The island
594 mass effect and biological carbon uptake for the subantarctic Crozet Archipelago, *Deep-Sea
595 Research Part II-Topical Studies in Oceanography*, 54(18-20), 2174-2190.

596 Bakker, D. C. E., M. Hoppema, M. Schröder, W. Geibert, and H. J. W. De Baar (2008), A rapid
597 transition from ice covered CO₂-rich waters to a biologically mediated CO₂ sink in the eastern
598 Weddell Gyre, *Biogeosciences*, 5, 1373–1386.

599 Bathmann, U. V., R. Scharek, C. Klaas, C. D. Dubischar, and V. Smetacek (1997), Spring
600 development of phytoplankton biomass and composition in major water masses of the Atlantic sector
601 of the Southern Ocean, *Deep-Sea Research Part II-Topical Studies in Oceanography*, 44(1-2), 51-67.

602 Behrenfeld, M. J., and P. G. Falkowski (1997), Photosynthetic rates derived from satellite-based
603 chlorophyll concentration, *Limnology and Oceanography*, 42(1), 1-20.

604 Berger, W. H. (1989), Appendix: Global Maps of Ocean Productivity, in *Productivity of the Ocean: Present and Past*, edited by W. H. Berger, V. S. Smetacek and G. Wefer, pp. 429-455, John Wiley and Sons Limited.

605

606

607 Blain, S., et al. (2007), Effect of natural iron fertilization on carbon sequestration in the Southern

608 Ocean, *Nature*, 446(7139), 1070-U1071.

609 Boyd, P. W., et al. (2007), Mesoscale iron enrichment experiments 1993-2005: Synthesis and future

610 directions, *Science*, 315(5812), 612-617.

611 Boye, M., C. M. G. van den Berg, J. T. M. de Jong, H. Leach, P. Croot, and H. J. W. de Baar (2001),

612 Organic complexation of iron in the Southern Ocean, *Deep-Sea Research Part I-Oceanographic*

613 *Research Papers*, 48(6), 1477-1497.

614 Charlson, R. J., J. E. Lovelock, M. O. Andreae, and S. G. Warren (1987), Oceanic Phytoplankton,

615 Atmospheric Sulfur, Cloud Albedo and Climate, *Nature*, 326(6114), 655-661.

616 Cochran, J. K., and P. Masque (2003), Short-lived U/Th series radionuclides in the ocean: Tracers for

617 scavenging rates, export fluxes and particle dynamics, in *Uranium-Series Geochemistry*, edited, pp.

618 461-492, Mineralogical Soc America, Washington.

619 Croot, P. L., K. Andersson, M. Ozturk, and D. R. Turner (2004), The distribution and speciation of

620 iron along 6 degrees E in the Southern Ocean, *Deep-Sea Research Part II-Topical Studies in*

621 *Oceanography*, 51(22-24), 2857-2879.

622 Culberson, C. H. (1991), Dissolved oxygen. WOCE Operations Manual. WHP Operations and

623 Methods., in *WHP Office Report WHPO 91-1*, edited, pp. Section 3.1, Part 3.1.3, Woods Hole, Mass.

624 de Steur, L., D. M. Holland, R. D. Muench, and M. G. McPhee (2007), The warm-water "Halo"

625 around Maud Rise: Properties, dynamics and Impact, *Deep-Sea Research Part I-Oceanographic*

626 *Research Papers*, 54(6), 871-896.

627 Eicken, H. (1992), Salinity Profiles of Antarctic Sea Ice - Field Data and Model Results, *Journal of*

628 *Geophysical Research-Oceans*, 97(C10), 15545-15557.

629 Francois, R., M. A. Altabett, E. F. Yu, D. M. Sigman, M. P. Bacon, M. Frank, G. Bohrmann, G.

630 Bareille, and L. D. Labeyrie (1997), Contribution of Southern Ocean surface-water stratification to

631 low atmospheric CO₂ concentrations during the last glacial period, *Nature*, 389(6654), 929-935.

632 Garibotti, I.A. Vernet, M. Kozlowski, W.A. Ferrario M.E. (2003) Composition and biomass of

633 phytoplankton assemblages in coastal Antarctic waters: a comparison of chemotaxonomic and

634 microscopic analyses, *Marine Ecology Progress Series* 247, 27-42.

635 Geibert, W., and I. Vöge (2008), Progress in the determination of ²²⁷Ac in sea water, *Marine*

636 *Chemistry*, 109(3-4), 238-249.

637 Geibert, W., M. M. Rutgers van der Loeff, C. Hanfland, and H. J. Dauelsberg (2002), Actinium-227

638 as a deep-sea tracer: Sources, distribution and applications, *Earth and Planetary Science Letters*,

639 198(1-2), 147-165.

640 Geibert, W., M. M. Rutgers van der Loeff, R. Usbeck, R. Gersonde, G. Kuhn, and J. Seeberg-

641 Elverfeldt (2005), Quantifying the opal belt in the Atlantic and southeast Pacific sector of the

642 Southern Ocean by means of ²³⁰Th normalization, *Global Biogeochemical Cycles*, 19(4).

643 Geibert, W., M. Charette, G. Kim, W. S. Moore, J. Street, M. Young, and A. Paytan (2008), The

644 release of dissolved actinium to the ocean: A global comparison of different end-members, *Marine*

645 *Chemistry*, 109(3-4), 409-420.

646 Gladstone, R. M., G. R. Bigg, and K. W. Nicholls (2001), Iceberg trajectory modeling and meltwater

647 injection in the Southern Ocean, *Journal of Geophysical Research-Oceans*, 106(C9), 19903-19915.

648 Gordon, A. L., and B. A. Huber (1990), Southern-Ocean Winter Mixed Layer, *Journal of*

649 *Geophysical Research-Oceans*, 95(C7), 11655-11672.

650 Gouretski, V. V., and A. I. Danilov (1993), Weddell Gyre - Structure of the Eastern Boundary, *Deep-*

651 *Sea Research Part I-Oceanographic Research Papers*, 40(3), 561-582.

652 Grasshoff, K. K., K.; Ehrhardt, M. (1983), *Methods of Seawater Analysis*, 2 ed., Verlag Chemie,
653 Weinheim, Deerfield Beach.

654 Hegner, E., H. J. Dauelsberg, M. M. R. van der Loeff, C. Jeandel, and H. J. W. de Baar (2007), Nd
655 isotopic constraints on the origin of suspended particles in the Atlantic sector of the Southern Ocean,
656 *Geochemistry Geophysics Geosystems*, 8.

657 Helmke, P., O. Romero, and G. Fischer (2005), Northwest African upwelling and its effect on
658 offshore organic carbon export to the deep sea, *Global Biogeochemical Cycles*, 19(4).

659 Hoppema, M. (2004), Weddell Sea is a globally significant contributor to deep-sea sequestration of
660 natural carbon dioxide, *Deep Sea Research Part I: Oceanographic Research Papers*, 51(9), 1169-
661 1177.

662 Hoppema, M., and L. Goeyens (1999), Redfield behavior of carbon, nitrogen, and phosphorus
663 depletions in Antarctic surface water, *Limnology and Oceanography*, 44(1), 220-224.

664 Hoppema, M., H. J. W. de Baar, R. G. J. Bellerby, E. Fahrbach, and K. Bakker (2002), Annual export
665 production in the interior Weddell Gyre estimated from a chemical mass balance of nutrients, *Deep*
666 *Sea Research Part II: Topical Studies in Oceanography*, 49(9-10), 1675-1689.

667 Hutchins, D. A., and K. W. Bruland (1998), Iron-limited diatom growth and Si : N uptake ratios in a
668 coastal upwelling regime, *Nature*, 393(6685), 561-564.

669 Johnson, K. S. (2001), Iron supply and demand in the upper ocean: Is extraterrestrial dust a
670 significant source of bioavailable iron?, *Global Biogeochemical Cycles*, 15(1), 61-63.

671 Jongma, J. I., E. Driesschaert, T. Fichfet, H. Goosse, and H. Renssen (2009), The effect of dynamic-
672 thermodynamic icebergs on the Southern Ocean climate in a three-dimensional model, *Ocean*
673 *Model.*, 26(1-2), 104-113.

674 Kang, S. H., and G. A. Fryxell (1993), Phytoplankton in the Weddell Sea, Antarctica - Composition,
675 Abundance and Distribution in Water-Column Assemblages of the Marginal Ice-Edge Zone During
676 Austral Autumn, *Mar. Biol.*, 116(2), 335-348.

677 Kattner, G. (1999), Storage of dissolved inorganic nutrients in seawater: poisoning with mercuric
678 chloride, *Marine Chemistry*, 67(1-2), 61-66.

679 Kimura, N. (2004), Sea ice motion in response to surface wind and ocean current in the Southern
680 Ocean, *J. Meteorol. Soc. Jpn.*, 82(4), 1223-1231.

681 Kirk, J. T. O. (1994), *Light & Photosynthesis in Aquatic Ecosystems*, Cambridge University Press.

682 Lannuzel, D., V. Schoemann, J. de Jong, J. L. Tison, and L. Chou (2007), Distribution and
683 biogeochemical behaviour of iron in the East Antarctic sea ice, *Marine Chemistry*, 106(1-2), 18-32.

684 Lannuzel, D., V. Schoemann, J. de Jong, L. Chou, B. Delille, S. Becquevort, and J. L. Tison (2008),
685 Iron study during a time series in the western Weddell pack ice, *Marine Chemistry*, 108(1-2), 85-95.

686 Leynaert, A., D. M. Nelson, B. Queguiner, and P. Treguer (1993), The Silica Cycle in the Antarctic
687 Ocean - Is the Weddell Sea Atypical, *Marine Ecology-Progress Series*, 96(1), 1-15.

688 Lichey, C., and H. H. Hellmer (2001), Modeling giant-iceberg drift under the influence of sea ice in
689 the Weddell Sea, Antarctica, *J. Glaciol.*, 47(158), 452-460.

690 Marinov, I., A. Gnanadesikan, J. R. Toggweiler, and J. L. Sarmiento (2006), The Southern Ocean
691 biogeochemical divide, *Nature*, 441(7096), 964-967.

692 Martínez-García, A., A. Rosell-Melé, W. Geibert, V. Gaspari, P. Masqué, R. Gersonde, and C.
693 Barbante (2009), Links between Fe supply, ocean productivity, sea surface temperature and CO₂ over
694 the last 1.1My, *Paleoceanography*, 24(PA1207).

695 Martinson, D. G., and R. A. Iannuzzi (2003), Spatial/temporal patterns in Weddell gyre
696 characteristics and their relationship to global climate, *Journal of Geophysical Research-Oceans*,
697 108(C4).

698 Meskhidze, N., A. Nenes, W. L. Chameides, C. Luo, and N. Mahowald (2007), Atlantic Southern
699 Ocean productivity: Fertilization from above or below?, *Global Biogeochemical Cycles*, 21(2).

700 Morel, A., and J. F. Berthon (1989), Surface Pigments, Algal Biomass Profiles, and Potential
701 Production of the Euphotic Layer - Relationships Reinvestigated in View of Remote-Sensing
702 Applications, *Limnology and Oceanography*, 34(8), 1545-1562.

703 Mueller, P. J., and R. Schneider (1993), An automated leaching method for the determination of opal
704 in sediments and particulate matter, *Deep-Sea Research Part I Oceanographic Research Papers*,
705 40(3), 425-444.

706 Nozaki, Y. (1984), Excess ²²⁷Ac in deep ocean water, *Nature*, 310, 486-488.

707 Nozaki, Y. (1993), Actinium-227: a steady state tracer for the deep-sea basin-wide circulation and
708 mixing studies, in *Deep ocean circulation, physical and chemical aspects*, edited by T. Teramoto, pp.
709 139-155, Elsevier.

710 Orsi, A. H., T. Whitworth, and W. D. Nowlin (1995), On the Meridional Extent and Fronts of the
711 Antarctic Circumpolar Current, *Deep-Sea Research Part I-Oceanographic Research Papers*, 42(5),
712 641-673.

713 Pichevin, L., B. C. Reynolds, R. Ganeshram, I. Cacho, L. Pena, K. Keefe, and R. M. Ellam (2009),
714 Enhanced Carbon Pump Inferred from Relaxation of Nutrient Limitation in the Glacial Ocean,
715 *Nature*, 459, 1114-1117.

716 Ragueneau, O., S. Schultes, K. Bidle, P. Claquin, and B. La Moriceau (2006), Si and C interactions
717 in the world ocean: Importance of ecological processes and implications for the role of diatoms in the
718 biological pump, *Global Biogeochemical Cycles*, 20(4).

719 Raiswell, R., L. G. Benning, M. Tranter, and S. Tulaczyk (2008), Bioavailable iron in the Southern
720 Ocean: the significance of the iceberg conveyor belt, *Geochem. Trans.*, 9.

721 Rutgers van der Loeff, M. M., and W. S. Moore (1999), Determination of natural radioactive tracers,
722 in *Methods of seawater analysis*, edited by K. K. Grasshoff, K.; Ehrhardt, M., pp. 365-397, Wiley-
723 VCH, Weinheim, New York, Chichester, Brisbane, Singapore, Toronto.

724 Savidge, G., J. Priddle, L. C. Gilpin, U. Bathmann, E. J. Murphy, N. J. P. Owens, R. T. Pollard, D. R.
725 Turner, C. Veth, and P. Boyd (1996), An assessment of the role of the marginal ice zone in the
726 carbon cycle of the Southern Ocean, *Antarct. Sci.*, 8(4), 349-358.

727 Savoye, N., C. Benitez-Nelson, A. B. Burd, J. K. Cochran, M. Charette, K. O. Buesseler, G. A.
728 Jackson, M. Roy-Barman, S. Schmidt, and M. Elskens (2006), Th-234 sorption and export models in
729 the water column: A review, *Marine Chemistry*, 100(3-4), 234-249.

730 Schlitzer, R. (2002), Carbon export fluxes in the Southern Ocean: results from inverse modeling and
731 comparison with satellite-based estimates, *Deep-Sea Research Part II-Topical Studies in*
732 *Oceanography*, 49(9-10), 1623-1644.

733 Schlitzer, R. (2008): Software Ocean Data View. <http://odv.awi.de>.

734 Schodlok, M. P., H. H. Hellmer, J. schwarz, and T. Busche (2005), On iceberg behaviour:
735 observations, model results, and satellite data. Forum for Research into Ice Shelf Processes
736 (FRISP)Rep. 16, 19-25 pp.

737 Schodlok, M. P., H. H. Hellmer, G. Rohardt, and E. Fahrbach (2006), Weddell Sea iceberg drift: Five
738 years of observations, *Journal of Geophysical Research-Oceans*, 111(C6).

739 Schröder, M., and E. Fahrbach (1999), On the structure and the transport of the eastern Weddell
740 Gyre, *Deep-Sea Research Part II-Topical Studies in Oceanography*, 46(1-2), 501-527.

741 Schussler, U., and K. Kremling (1993), A Pumping System for Underway Sampling of Dissolved and
742 Particulate Trace-Elements in near-Surface Waters, *Deep-Sea Research Part I-Oceanographic*
743 *Research Papers*, 40(2), 257-266.

744 Schwarz, J. N., and M. P. Schodlok (2009), Impact of drifting icebergs on surface phytoplankton
745 biomass in the Southern Ocean: Ocean colour remote sensing and in situ iceberg tracking, *Deep-Sea*
746 *Research Part I Oceanographic Research Papers*, 56(10), 1727-1741.

747 Sigman, D. M., and E. A. Boyle (2000), Glacial/interglacial variations in atmospheric carbon dioxide,
748 *Nature*, 407(6806), 859-869.

749 Smetacek, V., C. Klaas, S. Menden-Deuer, and T. A. Ryneerson (2002), Mesoscale distribution of
750 dominant diatom species relative to the hydrographical field along the Antarctic Polar Front, *Deep-*
751 *Sea Research Part II-Topical Studies in Oceanography*, 49(18), 3835-3848.

752 Smith, K. L., B. H. Robison, J. J. Helly, R. S. Kaufmann, H. A. Ruhl, T. J. Shaw, B. S. Twining, and
753 M. Vernet (2007), Free-drifting icebergs: Hot spots of chemical and biological enrichment in the
754 Weddell Sea, *Science*, 317(5837), 478-482.

755 Smith, W. O., and D. M. Nelson (1985), Phytoplankton Bloom Produced by a Receding Ice Edge in
756 the Ross Sea - Spatial Coherence with the Density Field, *Science*, 227(4683), 163-166.

757 Smith, W. O., and J. C. Comiso (2008), Influence of sea ice on primary production in the Southern
758 Ocean: A satellite perspective, *Journal of Geophysical Research-Oceans*, 113(C5).

759 Sokolov, S. (2008), Chlorophyll blooms in the Antarctic Zone south of Australia and New Zealand in
760 reference to the Antarctic Circumpolar Current fronts and sea ice forcing, *Journal of Geophysical*
761 *Research-Oceans*, 113(C3).

762 Stephens, B. B., and R. F. Keeling (2000), The influence of Antarctic sea ice on glacial-interglacial
763 CO₂ variations, *Nature*, 404(6774), 171-174.

764 Sunda, W. G., and S. A. Huntsman (1995), Iron Uptake and Growth Limitation in Oceanic and
765 Coastal Phytoplankton, *Marine Chemistry*, 50(1-4), 189-206.

766 Takeda, S. (1998), Influence of iron availability on nutrient consumption ratio of diatoms in oceanic
767 waters, *Nature*, 393(6687), 774-777.

768 Tournadre, J., K. Whitmer, and F. Girard-Ardhuin (2008), Iceberg detection in open water by
769 altimeter waveform analysis, *Journal of Geophysical Research-Oceans*, 113(C8).

770 Tsuda, A., et al. (2003), A mesoscale iron enrichment in the western Subarctic Pacific induces a large
771 centric diatom bloom, *Science*, 300(5621), 958-961.

772 Twining, B.S., S.B. Baines, N.S. Fisher, and M.R. Landry (2004), Cellular iron contents of plankton
773 during the Southern Ocean Iron Experiment (SOFeX), *Deep-Sea Research I*, 51, 1827-1850.

774 Tynan, C. T. (1998), Ecological importance of the Southern Boundary of the Antarctic Circumpolar
775 Current, *Nature*, 392(6677), 708-710.

776 Uotila, J., T. Vihma, and J. Launiainen (2000), Response of the Weddell Sea pack ice to wind
777 forcing, *Journal of Geophysical Research-Oceans*, 105(C1), 1135-1151.

778 Usbeck, R., M. R. van der Loeff, M. Hoppema, and R. Schlitzer (2002), Shallow remineralization in
779 the Weddell Gyre, *Geochemistry Geophysics Geosystems*, 3.

780 Utermöhl, H. (1958), Zur Vervollkommnung der quantitativen Phytoplankton-Methodik,
781 *Mitteilungen der Int. Ver. Limnol.*, 9, 1-38.

782 Weller, R., J. Woltjen, C. Piel, R. Resenberg, D. Wagenbach, G. König-Langlo, and M. Kriews
783 (2008), Seasonal variability of crustal and marine trace elements in the aerosol at Neumayer station,
784 Antarctica, *Tellus Ser. B-Chem. Phys. Meteorol.*, 60(5), 742-752.

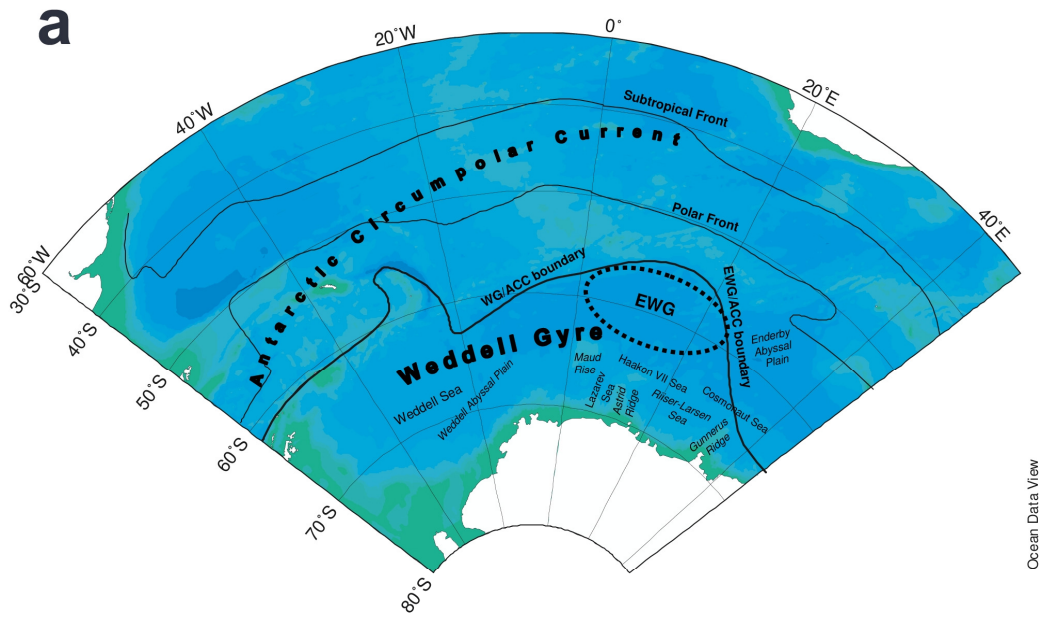
785 Worby, A. P., C. A. Geiger, M. J. Paget, M. L. Van Woert, S. F. Ackley, and T. L. DeLiberty (2008),
786 Thickness distribution of Antarctic sea ice, *Journal of Geophysical Research-Oceans*, 113(C5).

787 Wright, S. W., S. W. Jeffrey, R. F. C. Mantoura, C. A. Llewellyn, T. Bjornland, D. Repeta, and N.
788 Welschmeyer (1991), Improved Hplc Method for the Analysis of Chlorophylls and Carotenoids from
789 Marine-Phytoplankton, *Marine Ecology-Progress Series*, 77(2-3), 183-196.

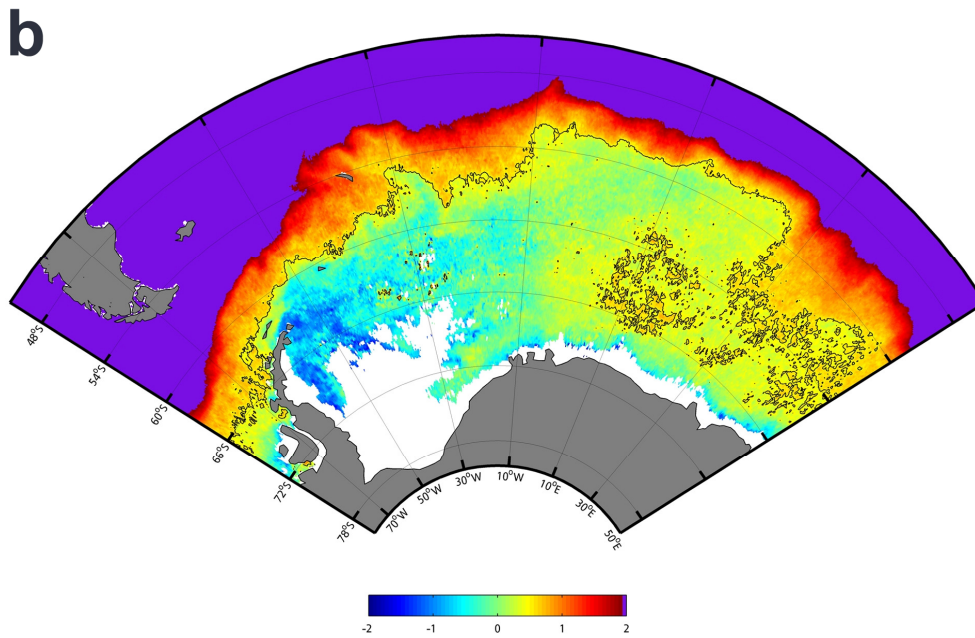
790
791
792 **Table 1: Estimates of production, freshwater input due to melting ice and concentration (activity) data**
793 **for the isotope ²²⁷Ac_{xs} at the sea surface. Methods and the associated uncertainties are discussed in**
794 **the text. PP (primary production) is given in units of C, Si production is given in units of Si.**

Station (PS63/)	Date (2003)	Lon °E	Lat °N	sea ice thickness equivalent [mm]	Si production from Si deficit [mmol/m ²]	PP from NO _x deficit [mmol/m ²]	PP from TCO ₂ deficit [mmol/m ²]	PP from in- situ chl-a, depth- integrated [mmol/m ²]	PP from in- situ chl-a 10 m VGPM (28 days) [mmol/m ²]	PP from MODIS VGPM (last 28 days) [mmol/m ²]	EP from ²³⁴ Th [mmol/m ²]	Fe/C [mol/mol]	²²⁷ Ac _{xs} ±1 σ (surface) [dpm/m ³]
119-01	06/01	17.76	-65.83	143	14	24		140	108	249			
120-02	07/01	18.49	-65.41	257	50	52		157	148	248			
121-02	07/01	19.02	-64.96	192	20	19		149	164	222	145	0.0002	0.38 ± 0.06
122-01	08/01	19.81	-64.56	171	4	2		149	230	220			
123-02	08/01	20.76	-64.13	585	184	214	26	114	59	211			
124-01	08/01	21.74	-63.75	413	264	364	32	203	96	251			
125-01	09/01	22.99	-63.50	340	201	275	103	169	149	276			
126-01	09/01	22.99	-63.00	591	405	609		164	76	406			
127-01	09/01	23.00	-62.50	622	349	859	344	350	108	700		0.0004	0.25 ± 0.05
128-01	09/01	22.99	-62.00	512	322	1254	1097				2018		
130-01	10/01	23.00	-61.50	563	446	1301	1187	724	690	903			
131-01	10/01	23.00	-61.00	665	446	1720	1740	939	326	1009	504		
133-01	10/01	23.02	-60.50	986	844	2113	1978	881	1119	926			
134-01	11/01	22.99	-59.96	1061	887	2020		806	547	614			
135-01	11/01	23.01	-59.50	1255	1022	2242	1344	546	1203	746	594		
137-01	12/01	23.01	-59.00	1341	639	2150	1928	599	1028	666			
138-01	12/01	23.00	-58.50	1292	804	2115	1593	618	666	614			
139-01	12/01	23.00	-58.31									0.0002	0.22 ± 0.06
140-01	12/01	22.99	-58.02	811	1090	2349	1065	589	844	529			
141-01	13/01	23.00	-57.51	895	1051	2022	1143	772	1024	674			
142-01	13/01	22.99	-57.01		932	2033	1567	706	153	771	905		
143-01	13/01	23.01	-56.50	515	919	2264	1519	988	701	741		0.0002	0.60 ± 0.07
144-01	14/01	23.00	-56.00	239	457	1640	954	473	579	747			
145-01	14/01	23.02	-55.51	234	600	1555	914	379	211	684			
146-01	14/01	23.00	-55.32									0.0002	0.98 ± 0.09
147-01	14/01	23.01	-55.01	105	281	1453	906	425	645	600	1116		
148-01	14/01	23.00	-54.50	228	136	1249	672	418	449	516			
149-01	15/01	23.05	-53.95	103	238	955	323	337	471	482			
150-01	15/01	23.01	-53.49	69	678	1693	1052	490	209	544			0.26 ± 0.05
152-01	15/01	22.99	-53.00		1877	1900	1248	624	570	592	1158	0.0002	0.58 ± 0.07

795
796
797
798



Ocean Data View

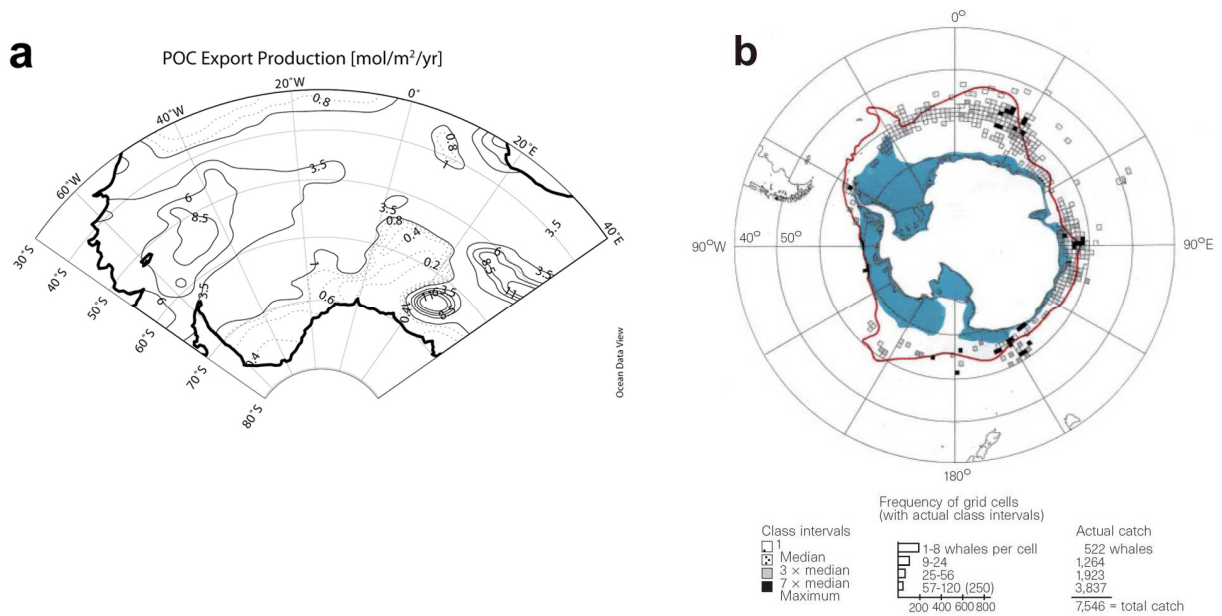


799

800 **Figure 1 (a) :Map of the bathymetry in the Atlantic Sector of the Southern Ocean, indicating**
 801 **oceanographic features (in bold fonts), topographic features (in italic fonts) and the names of regions**
 802 **(in normal fonts). Fronts and the ACC/WG boundary follow [A H Orsi et al., 1995] (b) The Weddell Gyre**
 803 **as seen in sea surface temperature (MODIS satellite instrument, composite of data from 2002 to 2008).**
 804 **The solid line indicates the 0.5 °C isotherm. Note the longitudinal temperature boundary at ~25°E.**

805

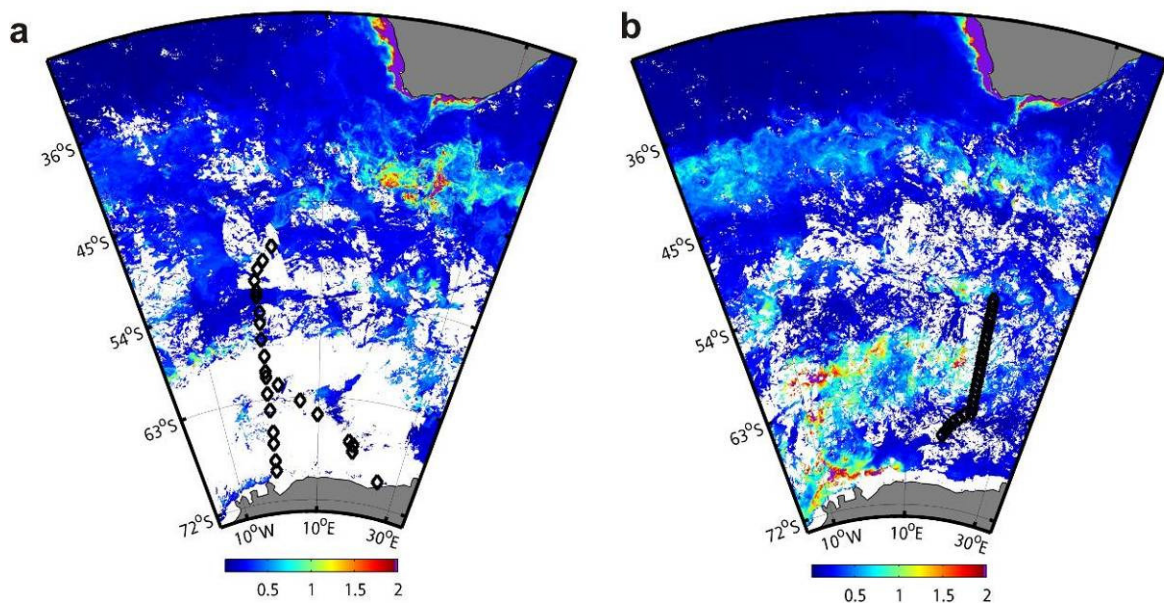
806



807
808
809

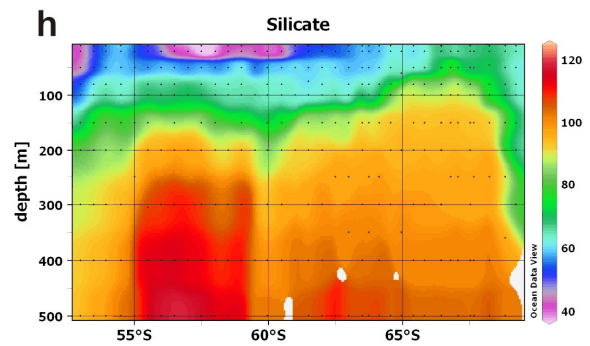
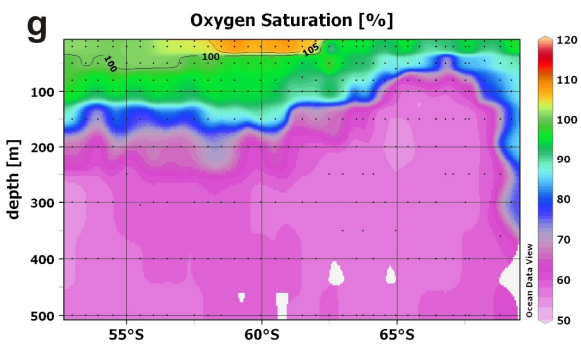
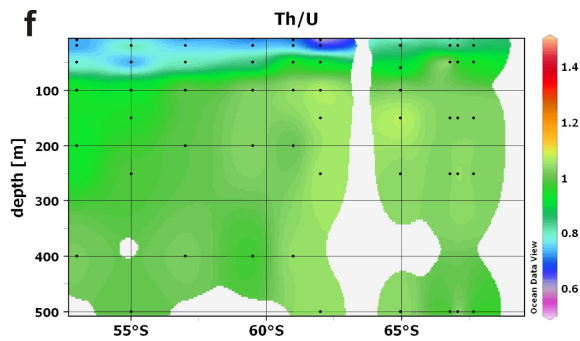
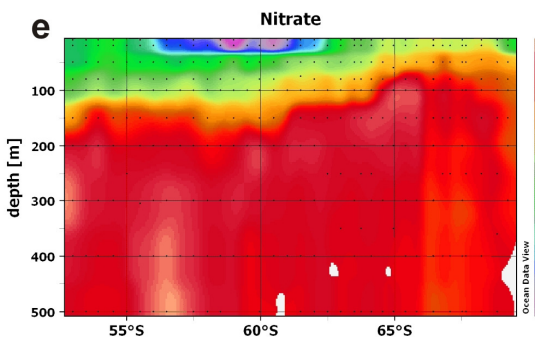
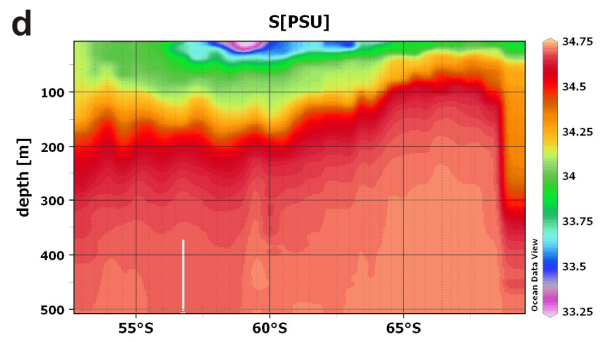
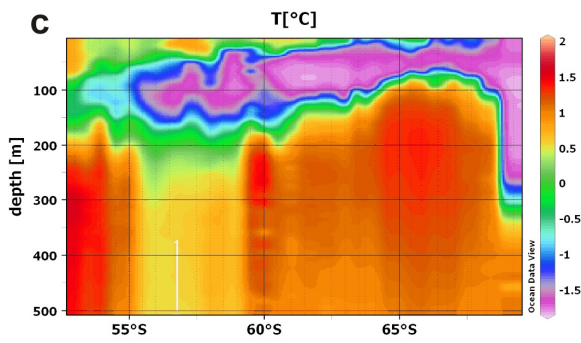
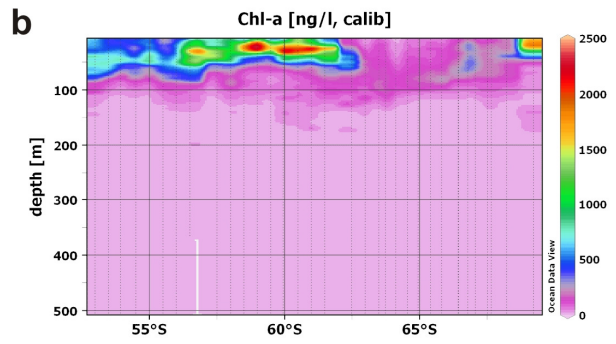
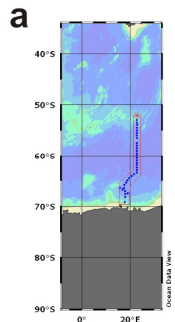
Figure 2: Indicators of bioproductivity in the WG. Left: Export production of Particulate Organic Carbon (POC) as derived by an inverse Global Circulation Model, POC export based on measured nutrient distributions, modified from [R Usbeck et al., 2002]. Right: Abundance of humpback whales, based on historical whale catch data [C T Tynan, 1998]. Reprinted by permission from Macmillan Publishers Ltd: nature 392(6677), 708-710, 1998 (www.nature.com). Blue whale catches (not shown here) display a similar pattern, but the maximum abundance is found further South. Both indicators point to substantial bioproductivity at the eastern rim of the WG, at approximately 23°E, 55-65°S

816



817

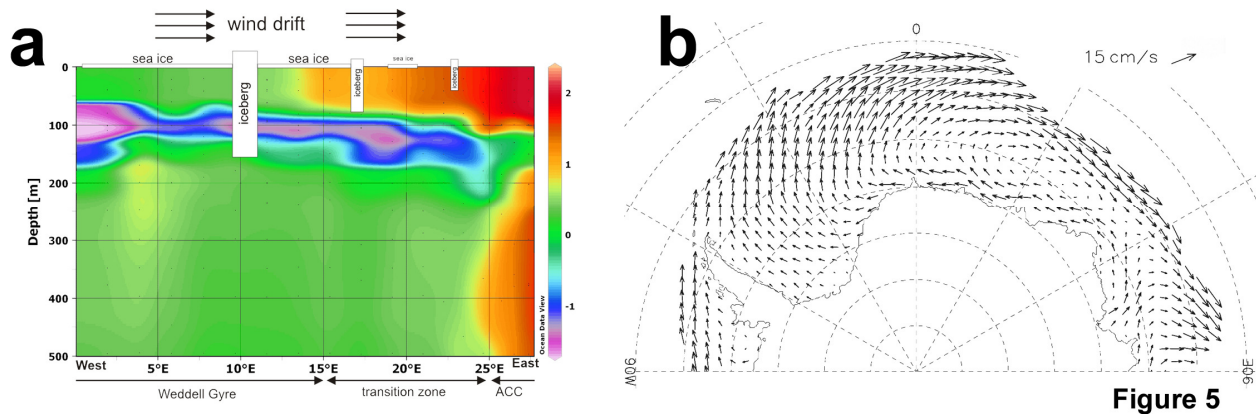
818 **Figure 3: Composites of sea surface chlorophyll concentration in $\text{mg}\cdot\text{m}^{-3}$ (NASA/SEAWiFS) during**
819 **ANT XX/2 in December 2002 (a) and January 2003 (b). Ship's stations are shown as open symbols.**
820 **White areas correspond to sea ice and/or clouds.**
821



822
823

824 **Figure 4: Results for a section along the EWG boundary (as indicated in a, together with bathymetry)**
 825 **in December 2002/January 2003. A substantial concentration of chl-a (b) is found between 62.5 S and**
 826 **57.5 °N. This signal is associated with a salinity minimum (d) and a surface temperature maximum (c),**
 827 **which indicate the role of melting ice. Nitrate [$\mu\text{mol/kg}$] (e) and silicate [$\mu\text{mol/kg}$] (h) are depleted due**
 828 **to phytoplankton growth, and $^{234}\text{Th}/^{238}\text{U}$ ratios <1 (f) indicate that particles have been exported from**
 829 **the surface layer. Oxygen saturation values $>100\%$ (g) are evidence of photosynthetic activity.**

830
831



832

833 **Figure 5 (a): Schematic drawing of the proposed mechanism for enhanced sea-ice and iceberg melting**
 834 **at the EWG/ACC boundary. Note that the underlying graph of temperature distribution is not based on**
 835 **data from this expedition, which were mainly oriented in the S-N direction, but were taken from World**
 836 **Ocean Circulation Experiment line SO4 (source: eWOCE). This transect is mostly W-E directed,**
 837 **following the prevailing wind direction in the Southern Ocean. The latitude ranges from $\sim 58^{\circ}\text{S}$ (W) to**
 838 **54°S (E). Our in-situ transect (Figure 3b, Figure 4) is oriented perpendicularly to this section,**
 839 **intersecting at 23°E . (b): Modified after [N Kimura, 2004]: Mean ice motion for 10 years in a polar**
 840 **stereographic projection. Sea-ice and enclosed icebergs will be forced eastwards by wind pressure,**
 841 **where they reach the warmer waters of the ACC, which float on top of WG WW. This causes enhanced**
 842 **melting of ice at the EWG/ACC boundary.**

843